Sensitivity and resolution improvement for in vivo magnetic resonance current-density imaging of the human brain

Göksu, Cihan; Scheffler, Klaus; Gregersen, Fróði; Eroğlu, Hasan H.; Heule, Rahel; Siebner, Hartwig R.; Hanson, Lars G.; Thielscher, Axel

Published in:
Magnetic Resonance in Medicine

Link to article, DOI:
10.1002/mrm.28944

Publication date:
2021

Document Version
Publisher's PDF, also known as Version of record

Received: 24 March 2021 | Revised: 6 July 2021 | Accepted: 8 July 2021

DOI: 10.1002/mrm.28944

RESEARCH ARTICLE

Magnetic Resonance in Medicine

Sensitivity and resolution improvement for in vivo magnetic resonance current-density imaging of the human brain

Cihan Göksu[1,2] | **Klaus Scheffler**[2,3] | **Fróði Gregersen**[1,4,5] | **Hasan H. Eroğlu**[1,4] | **Rahel Heule**[2,3] | **Hartwig R. Siebner**[1,6,7] | **Lars G. Hanson**[1,4] | **Axel Thielscher**[1,4]

[1]Danish Research Centre for Magnetic Resonance, Centre for Functional and Diagnostic Imaging and Research, Copenhagen University Hospital-Amager and Hvidovre, Copenhagen, Denmark

[2]High-Field Magnetic Resonance Center, Max-Planck-Institute for Biological Cybernetics, Tübingen, Germany

[3]Department of Biomedical Magnetic Resonance, University of Tübingen, Tübingen, Germany

[4]Center for Magnetic Resonance, DTU Health Tech, Technical University of Denmark, Kgs Lyngby, Denmark

[5]Sino-Danish Center for Education and Research, Aarhus, Denmark

[6]Department of Neurology, Copenhagen University Hospital, Bispebjerg, Denmark

[7]Institute for Clinical Medicine, Faculty of Medical and Health Sciences, University of Copenhagen, Copenhagen, Denmark

Correspondence
Cihan Göksu, Danish Research Centre for Magnetic Resonance, Centre for Functional and Diagnostic Imaging and Research, Copenhagen University Hospital Hvidovre, Section 714, Kettegaard Allé 30, 2650 Hvidovre, Denmark.
Email: cihang@drcmr.dk

Funding information
Lundbeck Foundation (grant nos. R288-2018-236 to C.G. and R244-2017-196 and R313-2019-622 to A.T.), the Max Planck Society, and the German Research Foundation (Reinhart Koselleck Project, grant no. DFG SCHE 658/12) is gratefully acknowledged. H.R.S. holds a 5-year professorship in precision medicine at the Faculty of Health Sciences and Medicine, University of Copenhagen, which is sponsored by the Lundbeck Foundation (grant no. R186-2015-2138).

Purpose: Magnetic resonance current-density imaging (MRCDI) combines MRI with low-intensity transcranial electrical stimulation (TES; 1-2 mA) to map current flow in the brain. However, usage of MRCDI is still hampered by low measurement sensitivity and image quality.

Methods: Recently, a multigradient-echo–based MRCDI approach has been introduced that presently has the best-documented efficiency. This MRCDI approach has now been advanced in three directions and has been validated by phantom and in vivo experiments. First, the importance of optimum spoiling for brain imaging was verified. Second, the sensitivity and spatial resolution were improved by using acquisition weighting. Third, navigators were added as a quality control measure for tracking physiological noise. Combining these advancements, the optimized MRCDI method was tested by using 1 mA TES for two different injection profiles.

Results: For a session duration of 4:20 min, the new MRCDI method was able to detect TES-induced magnetic fields at a sensitivity level of 84 picotesla, representing a twofold efficiency increase against our original method. A comparison between measurements and simulations based on personalized head models showed a consistent increase in the coefficient of determination of $\Delta R^2 = 0.12$ for the current-induced magnetic fields and $\Delta R^2 = 0.22$ for the current flow reconstructions. Interestingly, some of the simulations still clearly deviated from the measurements despite the strongly improved measurement quality. This highlights the utility of MRCDI to improve head models for TES simulations.

Lars G. Hanson and Axel Thielscher contributed equally to this work.

Conclusion: The achieved sensitivity improvement is an important step from proof-of-concept studies toward a broader application of MRCDI in clinical and basic neuroscience research.

KEYWORDS

acquisition-weighted in vivo brain imaging, current-induced magnetic field, magnetic resonance current-density imaging, navigators, spoiled multiecho-gradient echo

1 | INTRODUCTION

Magnetic resonance current-density imaging (MRCDI) and MR electrical impedance tomography (MREIT) are emerging modalities to measure the current flow of transcranial electric stimulation (TES)[1] and the ohmic tissue conductivities non-invasively in the human brain.[2,3,4-12] They combine MRI with weak electrical currents of 1 to 2 mA baseline-to-peak, alternating at low frequencies (0-100 Hz; Figure 1). The currents induce an alternating magnetic field in the brain, and its component $\Delta B_{z,c}$ parallel to the magnetic field of the MR scanner causes tiny modulations of the MR phase. MRCDI and MREIT aim to measure these phase modulations to gain insight into the strength and spatial distribution of the current-induced

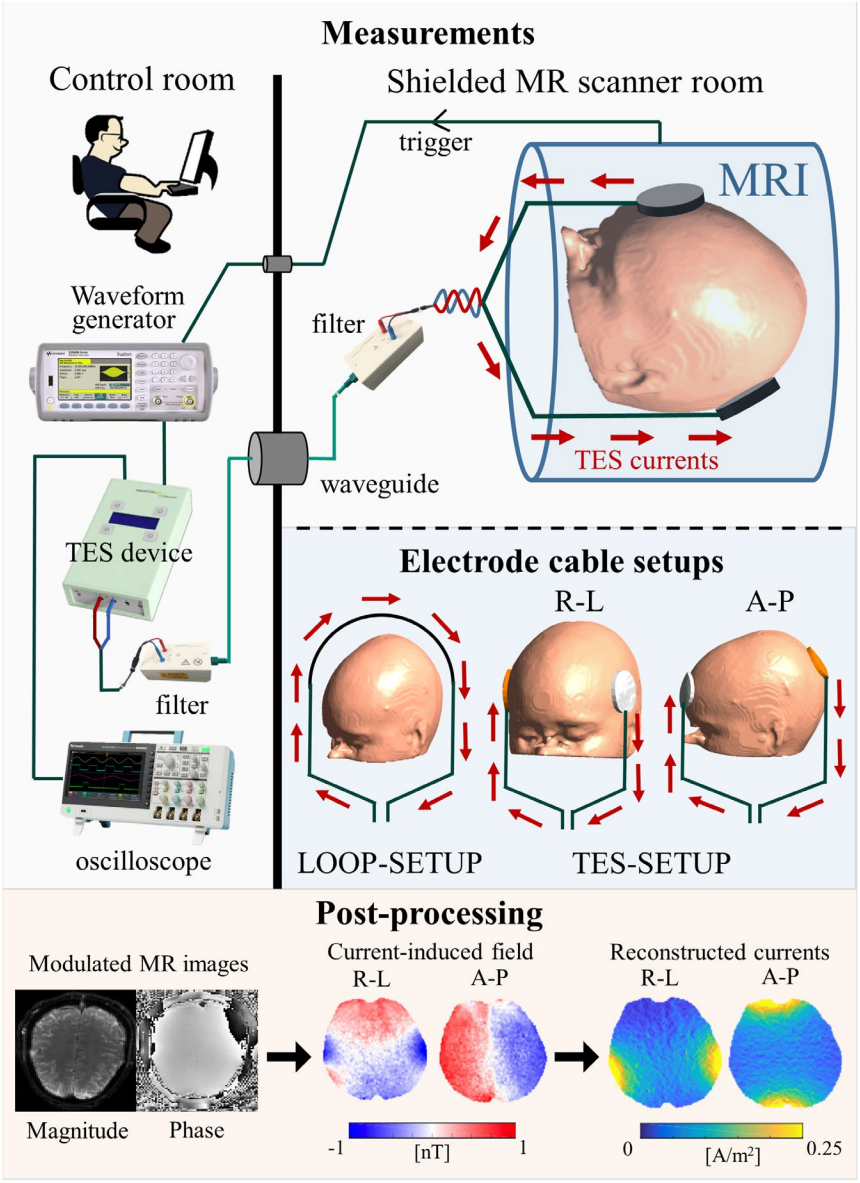

FIGURE 1 Experimental set-up for human in vivo brain magnetic resonance current-density imaging (MRCDI). The MR scanner sends a trigger signal to an arbitrary waveform generator (33500B; Keysight Technologies) in synchrony with the applied RF pulses. The generated voltage waveform determines the transcranial electrical stimulation (TES) current strength, pulse width, and polarity that are monitored with an oscilloscope. The voltage waveform is converted to electrical currents by a TES stimulator (DC-STIMULATOR MR, NeuroCare Group GmbH). The generated electrical currents are filtered from RF noise. Two different setups are used in this study. In the LOOP-SETUP, the currents are not injected into the head, but pass through a cable loop placed around the head. In the TES-SETUP, the TES currents are injected via scalp electrodes placed according to the desired current injection profile: right→left (R→L) or anterior→posterior (A→P)

magnetic field for informing reconstructions of the current flow and conductivity distributions. The approach has been successfully demonstrated in phantoms,[6,8,13-19] animals,[8,18,20-24] and human limbs in vivo,[8,18,25-28] but it is particularly challenging for the human brain because the current-induced magnetic field stays below 1 to 2 nT.[9,29-31] This is caused by the low maximal current strength that is tolerable and safe (1-2 mA),[32] and the "shielding" effect of the low-conductive skull, which results in part of the current being shunted through the scalp.

In prior proof-of-concept studies, we focused on optimization of the MR sequences,[9,10] and on correction of the impact of stray magnetic fields caused by the currents in the cables connected to the TES electrodes.[33] We established measurements of the current-induced magnetic field in the in vivo human brain at a sensitivity of approximately 0.1 nT in an approximate 9-minute scan.[9] Although promising, these early results indicated the need for further improvements: First, additional sensitivity enhancements of the $\Delta B_{z,c}$ measurements would be needed to obtain a good signal-to-noise ratio (SNR) in the reconstructed current flow and conductivity distributions. Second, the measurements were sensitive to physiological noise (eg, caused by subject movement), so that we occasionally had to exclude part of the data after visual inspection.[9] This pointed toward the need for developing an independent marker of the quality of the $\Delta B_{z,c}$ field measurements to amend the qualitative and subjective judgment. Third, in some $\Delta B_{z,c}$ images, artifacts close to the cables remained visible even after correcting for the cable stray fields (eg, see figure 4 in Göksu et al[33]). Further testing revealed that these artifacts were unlikely to stem mostly from inaccurate tracking of the cable paths, as initially thought, but rather pointed toward imperfect measurements.

In this study, we strongly improve our MRCDI approach based on gradient-echo imaging[9] to tackle the above challenges and systematically validate it in phantom and human in vivo experiments. We show that the improvements enable the reliable detection of magnetic field changes caused by the TES current flow in the human brain at a sensitivity level of 84 pT for a resolution of $2 \times 2 \times 3$ mm^3 and a 4:20-minute measurement duration.

2 | METHODS

2.1 | Subjects

We recruited eight healthy volunteers and performed four successive experiments, as described in detail below. One of the volunteers participated in each experiment, one in experiments 1 to 3, one in only experiment 1, and one in experiments 2 and 3. The remaining four volunteers participated only in the last experiment 4. The participants had no previous histories of neurological or psychiatric disorders and were screened for contraindications to MRI and TES. Written informed consent was obtained from all participants before the scans. The study complied with the Helsinki Declaration on Human Experimentation and was approved by the ethics committee of the medical faculty of the University of Tübingen, Germany and the Capital Region of Denmark.

2.2 | Measuring current-induced magnetic fields by gradient-echo MRI

All experiments were performed using 3T MR scanners (MAGNETOM Prisma, SIEMENS Healthcare) equipped with 64-channel head coils. The MR signals from each channel were combined with an adaptive-combine algorithm.[34] We employed a gradient-echo–based steady-state MRI pulse sequence[10] with constant tip-angle RF excitation pulses repeating at a constant time interval T_R and synchronized TES currents to create two steady-state magnetization states that are modulated by positive (+) and negative (−) current-induced magnetic fields (Supporting Information Figure S1). We used the steady-state MR signals acquired in each of the nth echo intervals to reconstruct a phase-difference image $\angle M_n^+ - \angle M_n^- = 2\gamma \Delta B_{z,c} T_E(n) + \Delta\varphi_{ss}$, where γ is the proton's gyromagnetic ratio, $T_E(n)$ the echo time, and $\Delta\varphi_{ss}$ the steady-state phase difference just after the excitation. Exploiting the linear dependence of $\Delta\varphi_{ss}$ on $\Delta B_{z,c}$ for tiny TES currents, we derived the corresponding image of the current-induced magnetic field change $\Delta B_{z,c}^n = \left(\angle M_n^+ - \angle M_n^-\right)/m_n$, where the slope m_n highly depends on the MR sequence and relaxation parameters (echo time $T_E(n)$, repetition time T_R, tip-angle α, the spoiling scheme; T_1, T_2, and T_2^*) and can numerically be calculated by integrating Bloch equations.[10,35,36]

The numerical slopes used for the $\Delta B_{z,c}^n$ measurements differ depending on the two spoiling techniques employed in our MRCDI sequence. First, we employed constant phase-RF excitation and systematically changed the spoiler gradient areas ensuring a different amount of intravoxel phase dispersions $\varphi_{sp} = [2\pi\text{-}32\pi]$ to test the impact of $\Delta\varphi_{ss}$ simulation accuracy on the $\Delta B_{z,c}$ measurements. Here, we estimated the slopes m_n based on constant nominal sequence parameters and approximate brain-tissue relaxation parameters at 3T similar to Göksu et al.[10] We also incorporated a T_2^* distribution obtained by fitting a perfectly spoiled gradient-echo MRI-signal model with a decaying exponential $M_{ss}(t) = M_{ss}(t=0) \cdot \exp\left(-T_E/T_2^*\right)$ to the acquired MR magnitude images. Second, we combined a strong spoiler gradient with a well-known RF-spoiling method that varies the phase of the jth applied RF pulses according to the phase-cycling scheme $\varphi_j = \varphi_{j-1} + j\varphi_0$ with $\varphi_0 = 50°$-phase increments.[37] Here, we used a nulled steady-state phase difference $\Delta\varphi_{ss} = 0$ in $\Delta B_{z,c}^n$ calculations assuming perfect spoiling.

Finally, each of the calculated $\Delta B^n_{z,c}$ images were systematically weighted and then combined to minimize the noise sensitivity of the combined $\Delta B_{z,c}$ image.[9,10,38] The underlying theory can be found in the Supporting Information. We corrected the combined $\Delta B_{z,c}$ images for the stray magnetic fields that are induced by cable currents similar to our previous study.[33] This involved cable tracking using an ultrashort T_E sequence and subtraction of the corresponding calculated fields.

2.3 | Measurement procedures and MRCDI experiments

We employed a transcranial electric stimulation device (DC-STIMULATOR MR; NeuroCare Group GmbH) in two different setups (Figure 1) using electrodes and cables that are made of low-conductivity silicone rubber (29.4 S/m) and optimized for MRCDI.[39] In the LOOP-SETUP, the generated currents were flowing in a cable loop placed around the head. In the TES-SETUP, the generated currents were injected into the head via round scalp electrodes for two different montages, anterior→posterior (A→P) and right→left (R→L). We employed 2-mA baseline-to-peak currents for the experiments using LOOP-SETUP and 1 mA for TES-SETUP and imaged two single slices in superior and inferior parts of the brain, respectively. The study was comprised of four successive experiments measuring the human brain in vivo:

1. We introduced an optimized spoiling scheme and tested how it influenced the MRCDI sensitivity and quality.
2. We tested the impact of acquisition weighting (AW) on the sensitivity and the resolution of the $\Delta B_{z,c}$ measurements and the accuracy of the current flow reconstructions.
3. We explored if undesired physiological MR-signal fluctuations can be tracked by navigators and used for data-quality assessment.
4. We compared our original[9] and improved MRCDI methods. The experiments were performed for two different electrode montages ensuring current injection profiles in A→P and in R→L directions.

We used the LOOP-SETUP in the experiments 1 to 3 and the TES-SETUP in experiment 4 (Figure 1). Experiments 1 and 2 were preceded by pilot experiments in phantoms, which are described in the Supporting Information.

2.3.1 | Experiment 1: Importance of proper spoiling in steady-state MRCDI

We used the LOOP-SETUP (Figure 1) to compare the sensitivity and accuracy of our gradient-echo–based MRCDI method for different spoiling schemes in three subjects. Imaging parameters were FOV = 224 × 183 mm^2, $\alpha = 30°$, $T_E = 5.6, 14.4, 23.2, 32, 40.8, 49.6$ ms, $T_R = 80$ ms, and an imaging matrix of 112 × 92. The measurements were repeated $N_{meas} = 16$ times to increase the SNR. The experiments were repeated for five different spoiler gradient strengths to ensure intravoxel phase dispersions of $\varphi_{sp} = 2\,\pi, 4\,\pi, 8\,\pi, 16\,\pi$, and $32\,\pi$ without RF spoiling, and the experiment with $\varphi_{sp} = 16\,\pi$ was then tested with RF spoiling.

2.3.2 | Experiment 2: Improving the spatial resolution and sensitivity by AW

We used the LOOP-SETUP to compare two different acquisition strategies in three subjects (standard vs AW; Figure 2A). We explored the influence of the point-spread function (PSF) quality on $\Delta B_{z,c}$ measurements and tested the impact of AW on the sensitivity and resolution of the MRCDI measurements. The total scan time was kept close to 4:20 min for both acquisition strategies. Imaging parameters were FOV = 224 × 183 mm^2, $\alpha = 30°$, $T_E = 5.6, 14.4, 23.2, 32, 40.8, 49.6, 58.4, 67.2$ ms, $T_R = 80$ ms, and combined $\varphi_{sp} = 16\,\pi$ and RF spoiling:

- Standard acquisition. We employed a standard k-space acquisition scheme in a finite-rectangular window corresponding to a preset nominal resolution $\Delta_{pe} = 2$ mm in the phase encoding direction and kept the total number of repetitions identical $N_{meas} = 16$ for each of the phase-encoding lines—uniform weighting (this acquisition scheme results in the standard sinc-shaped PSF that is known to cause ringing artifacts). An imaging matrix of 112 × 92 was used.
- Acquisition weighting. As a second strategy, we employed AW, ensuring an SNR-efficient PSF improvement.[40,41] The k-space data was acquired in an approximately 1.6-times broader window and filtered with a Hanning window ($h\left(k_{pe}\right) = \beta_p\left(1 + \cos\left(2\pi k_{pe}\Delta_{pe}/\beta_w\right)\right)/2$, where $\beta_w = 1.6$ determines the width of the filter, and $\beta_p = 1.2$ the peak value) in both phase-encoding and readout directions. The number of measurements was modified systematically to match the applied filter in the phase-encoding direction, which ensured a near-flat noise power after filtering (Figure 2A). An imaging matrix of 176 × 144 was used to match the actual resolutions of both cases.

2.3.3 | Experiment 3: Using navigators for data-quality assessment

To enable the continuous tracking of global field fluctuations caused by physiological noise and subject motion, we

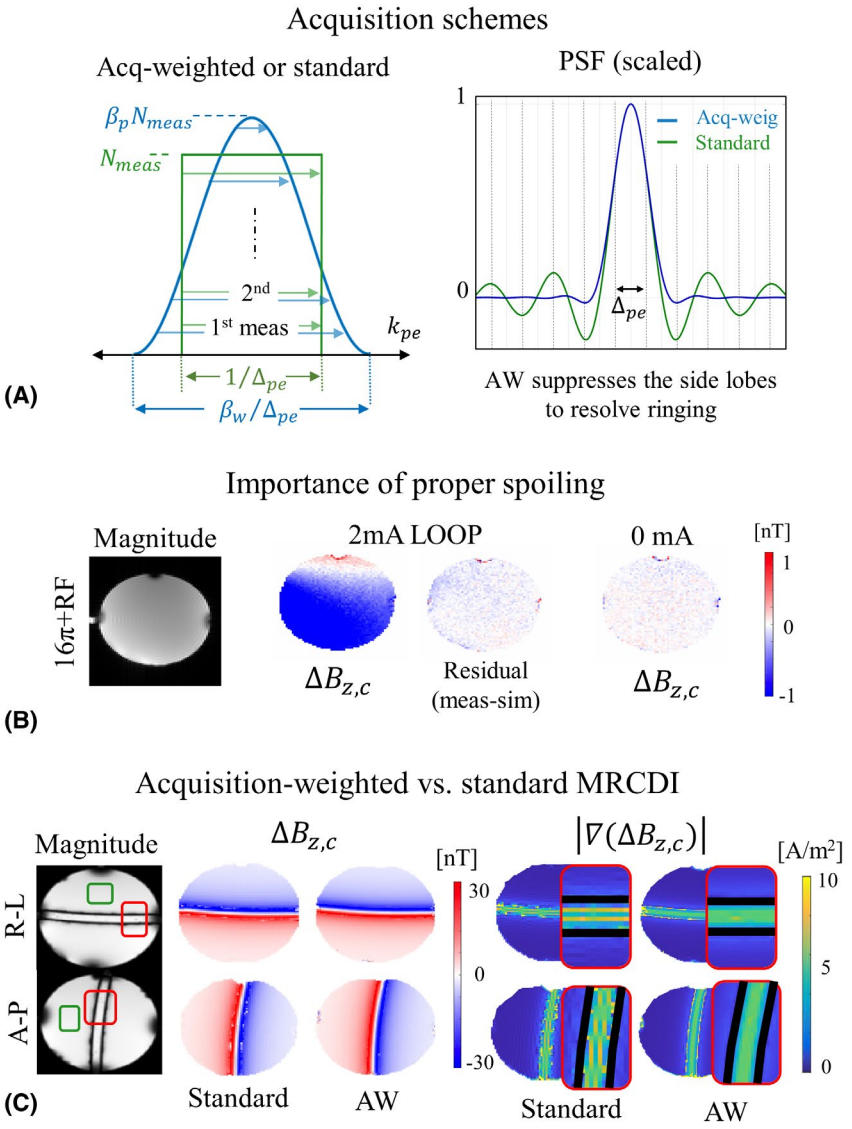

FIGURE 2 A, Unlike standard acquisition, the center of the k-space is measured more frequently than outer k-space for acquisition-weighted (AW) MRI. The weights are matched with the post hoc filter to resolve the ringing in the MR images by suppressing the side lobes in the PSF, while preserving the spatial resolution Δ_{pe} and SNR. Phantom experiments. B, Images of $\Delta B_{z,c}$ and its noise floor in a phantom acquired with the combination of RF and 16-π gradient spoiling For details, see experiment S.1 in the Supporting Information. C, Combined MR magnitude images for standard and AW acquisitions for a spherical phantom with a cylindrical tube (see experiment S.2 in the Supporting Information for details). The tube is aligned in a right→left (R→L) or anterior-posterior (A→P) direction. The impact of a better PSF is barely visible in the MR magnitude images (the green rectangles show the regions used for SNR calculations reported in Supporting Information Table S2; the red rectangles show the positions of the zoomed regions). The $\Delta B_{z,c}$ images and their normalized gradients $\left|\nabla\left(\Delta B_{z,c}\right)\right|$. The signal-void tube is concealed with black rectangles. MRCDI, magnetic resonance current-density imaging

modified the acquisition-weighted sequence of experiment 2 and replaced the first echo within every T_R with a 0-D navigator, while keeping the other parameters unchanged. We quantified the resulting SNR decrease by reanalyzing the data acquired in experiment 2, but discarded the first echo. Then, we used the LOOP-SETUP in three subjects to test whether the navigator signal could successfully track intentional jaw movements.

2.3.4 | Experiment 4: Human in vivo brain MRCDI for two different current-injection profiles

We compared the improved MRCDI method against our original method[9] that to our knowledge provides the best current-induced field measurement efficiency in vivo documented in the literature so far (~0.1 nT in a ~9-minute scan). We performed experiments (Figure 1; TES-SETUP; 1 mA) in five

subjects for two different current injection profiles in the A→P and R→L directions. Our original MRCDI method parameters were number of measurement repetitions $N_{meas} = 36$ (here reduced to 18 because of total scan-time restrictions), $T_R = 80$ ms, number of gradient echoes $N_{GE} = 5$, $T_E = 7.5$, 19.8, 31.9, 44, 56.2 ms, $\alpha = 30°$, spoiler gradient $\varphi_{sp} = 4\pi$, imaging matrix 112×90, voxel size $2 \times 2 \times 3$ mm^3. A chemical-shift–selective fat-suppression technique was applied in the experiment.[42]

The improved method with AW was used as described above for experiment 2. The first echo was replaced with a 0-D navigator. We did not perform fat suppression as multiple gradient-echo acquisition entails a sufficiently high bandwidth; instead, we used the period for acquisition of extra echoes. Both experiments with our original and improved method used single-slice measurements with the same FOV = 224 × 183 mm^2 and the total scan times kept at approximately 4:20 min for direct comparison of the sensitivity and resolution. In this study, none of the measurements were discarded because no abnormal signal fluctuations were observed in the navigator signals.

2.4 | Noise floor measurements in the $\Delta B_{z,c}$ images

In each of the experiments, $\Delta B_{z,c}$ control measurements without any current injections were performed and used to calculate the noise floors. For the phantom experiments, a mostly homogeneous region-of-interest (ROI) was selected, and a Gaussian distribution was fitted to the $\Delta B_{z,c}$ measurements to evaluate the SDs analogous to our previous study.[9] The accuracy of the used noise floor estimation method was validated for the phantom experiments by means of a direct comparison with theoretically calculated noise floors obtained from MR magnitude SNR[2,43,44] (please see Supporting Information Figure S4 and Tables S1 and S2). The noise floors were calculated in the entire brain tissue masks for the human in vivo case.

2.5 | Simulating the magnetic fields caused by cable currents

Before the MRCDI measurements, a 3D high-resolution structural scan based on the pointwise encoding time reduction with radial acquisition (PETRA) sequence[45] with the parameters as established in Göksu et al[9] and Göksu et al,[33] was performed to delineate the cable paths.

In the MRCDI experiments performed with LOOP-SETUP, the fully delineated cable path was used to simulate the expected $\Delta B_{z,c}$ fields based on the Biot-Savart law similar to our previous studies.[9,33] The simulated $\Delta B_{z,c}$ fields were subtracted from the measurements to obtain the residual $\Delta B_{z,c}$ images that are ideally zero. The residuals were then compared with the control measurements of the noise floor for no current injection. In the MRCDI experiments with TES-SETUP, the delineated cable paths up until the center of the scalp electrodes were used to simulate and correct for the stray magnetic fields caused by the cable currents.

2.6 | FEM simulations of the current flows and current-induced magnetic fields

For each participant in experiment 4, we performed additional high-resolution T_1- and T_2-weighted structural scans to inform personalized finite element method (FEM) simulations of the TES current flow and the current-induced magnetic fields (see Göksu et al[9] for the MR-sequence details). The structural scans were used to create volume conductor models using the headreco pipeline[46] in the open-source software SimNIBS 3 (www.simnibs.org; see Thielscher et al[47]). The models were composed of five tissue compartments differing in their ohmic conductivities[48,49]: Gray matter (GM; 0.275 S/m), white matter (WM; 0.126 S/m), CSF (1.654 S/m), skull (0.010 S/m), and scalp (0.465 S/m). The positions of the rubber TES electrodes were determined from the PETRA measurements. The electrodes (29.4 S/m) were modeled as discs with 5-mm thickness, 50-cm diameter. The thickness of the gel layers (0.37 S/m) between the electrodes and the scalp were determined from the PETRA images. Dirichlet boundary conditions for the electrostatic potential were applied at the electrode surfaces.[50] The current-flow distributions for A→P and R→L current-injection profiles were simulated for 1-mA current injections, and the 3D current-flow simulations were then used to calculate the current-induced magnetic field $\Delta B_{z,c}$ distributions based on Biot-Savart simulations.[51]

2.7 | Current flow reconstructions

A uniform conductivity of 1 S/m was assigned to the electrode pads, gel layer, and all compartments of the head models for the subjects in experiment 4 to obtain $\vec{J}_0$ and $\Delta B^0_{z,c}$. The projected current densities $\vec{J}_{rec} = \vec{J}_0 + \frac{1}{\mu_0}\left(\frac{\partial\left(\Delta B_{z,c} - \Delta B^0_{z,c}\right)}{\partial y}, -\frac{\partial\left(\Delta B_{z,c} - \Delta B^0_{z,c}\right)}{\partial x}, 0\right)$ were then reconstructed for the $\Delta B_{z,c}$ measurements and also for the $\Delta B_{z,c}$ simulations with literature conductivity values.[52,53] We used a median filter of 3 × 3 to eliminate high-frequency noise in the $\Delta B_{z,c}$ measurements, and the central difference approximation for the directional derivative operations in the reconstruction algorithm. The current flow reconstructions based on the measurements with our original and improved method were compared in terms of quality.

As the reconstruction approach employs spatial gradient operations on the measured $\Delta B_{z,c}$ image, we visualized the norm of its gradient $\left|\nabla\left(\Delta B_{z,c}\right)\right|$ as an additional quality index when comparing different measurements taken with the LOOP-SETUP.

3 | RESULTS

3.1 | Subject sensations

In the experiments with LOOP-SETUP, none of the subjects reported any side effects or discomfort. In the experiment 4 employing TES, all subjects reported phosphenes and a slight tingling sensation near the electrodes that disappeared after a short time for both electrode montages A→P and R→L. None of the subjects reported any further discomfort caused by TES.

3.2 | Experiment 1: Importance of proper spoiling in steady-state MRCDI

Tests in phantoms performed before human experiments (experiment S.1 in the Supporting Information) revealed that the combination of RF spoiling and gradient spoiling with φ_{sp} = 16 π showed the lowest noise floors. Also, the residual noise floors were in the same range as for the control measurements (Figure 2B), showing the importance of proper spoiling.

The results for the original and new spoiling schemes are exemplarily shown in Figure 3A for the first subject. No

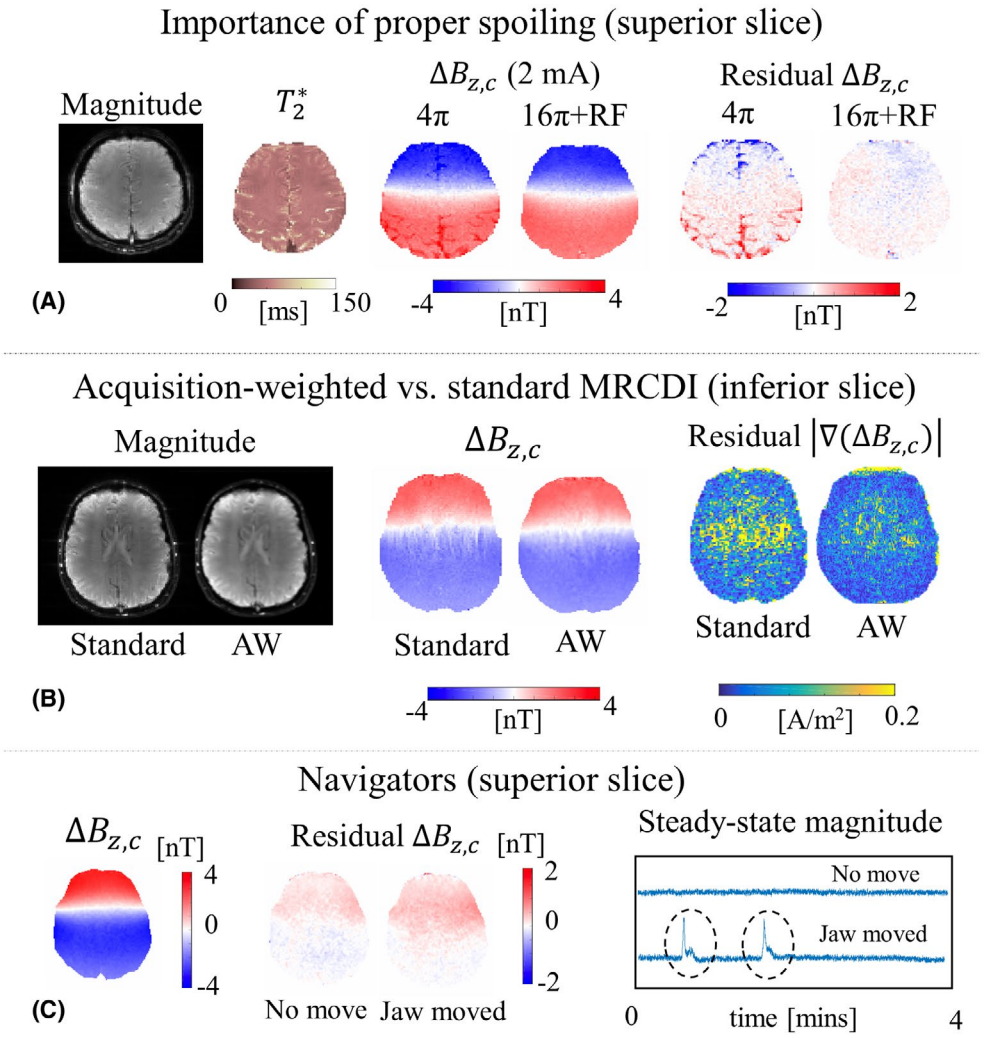

FIGURE 3 Results for the first subjects in experiments 1 to 3. A, Experiment 1: MR magnitude and T_2^* images exemplary shown for the combination of RF and φ_{sp} = 16-π spoiling. T_2^* is found to be significantly higher in CSF regions compared with brain tissue. $\Delta B_{z,c}$ measurements and residual images (ideally zero) clearly depict erroneous $\Delta B_{z,c}$ fields in CSF regions for the φ_{sp} = 4-π spoiling of our original method, likely caused by steady-state modeling errors. Combined RF and φ_{sp} = 16-π spoiling resolves this problem. B, Experiment 2: Employing acquisition-weighted (AW) MRI improves the quality of the MR magnitude and $\Delta B_{z,c}$ images compared with the standard acquisition scheme (ringing-caused fluctuations are suppressed by means of AW). Images of the norm of the gradient $\left|\nabla\left(\Delta B_{z,c}\right)\right|$ obtained from $\Delta B_{z,c}$ residuals (ideally zero) more clearly show the improvement in the noise floors for the AW measurements. C, Experiment 3: Navigator measurements when the subject performs no intentional movement (No move) or intentional jaw movement twice during the scan (Jaw moved). No obvious quality changes are visible in the $\Delta B_{z,c}$ measurements, but the noise floors increase with jaw movement (Table 1). The MR magnitude signal acquired from the navigator clearly fluctuates during jaw movements, and otherwise stays constant (note that the first 8 s are not plotted as the MR magnitude enters steady-state within this period). MRCDI, magnetic resonance current-density imaging

severe artifacts are observed in any of the MR magnitude images. However, gradient spoiling with $\varphi_{sp} = 4\ \pi$ results in erroneous $\Delta B_{z,c}$ fields in CSF regions, likely caused by steady-state modeling errors. These errors are resolved by the optimized spoiling (16 π and RF). The SDs of the residual $\Delta B_{z,c}$ images are listed in Table 1 to quantify the noise floors in all three subjects. In case of optimal spoiling (16 π and RF), the SDs were only slightly increased by 7% when compared against the control measurements without any currents. In summary, correcting the cable-induced stray fields works very well when proper spoiling is applied, and hardly impacts the noise floor in the corrected images (see the Supporting Information Figure S5 for all subjects).

3.3 | Experiment 2: Improving the spatial resolution and sensitivity by AW

AW tests in phantoms (experiment S.2 in the Supporting Information) showed a significant SNR and image-quality improvement in the $\Delta B_{z,c}$ images, for example, removal of spurious bright spots in the $\Delta B_{z,c}$ image close to the tubes (Figure 2C). The improvements in spatial resolution are clearly observed in the normalized gradient images $\left|\nabla\left(\Delta B_{z,c}\right)\right|$: The spatial derivative operation relevant for MRCDI reconstruction amplifies the ringing for standard acquisition, but this is resolved in the results obtained with AW (Figure 2A,C).

TABLE 1 The average SDs of $\Delta B_{z,c}$ images and their SDs across three subjects are given in picotesla [pT]

Experiment 1: std($\Delta B_{z,c}$) in [pT]						
Spoiling	**2 π**	**4 π**	**8 π**	**16 π**	**32 π**	**16 π + RF**
Superior						
Residual	200 ± 8	198 ± 9	198 ± 17	176 ± 7	175 ± 25	140 ± 4
Inferior						
Residual	204 ± 7	206 ± 11	212 ± 35	161 ± 9	171 ± 12	156 ± 7
Control	140 ± 9	149 ± 9	166 ± 20	144 ± 8	147 ± 7	143 ± 13

Experiment 2: std($\Delta B_{z,c}$) in [pT]				
Slice	**Inferior**		**Superior**	
method	**standard**	**AW**	**standard**	**AW**
Residual	131 ± 3	102 ± 7	142 ± 10	120 ± 13
Control	136 ± 5	120 ± 21	107 ± 19	73 ± 8

Experiment 3: std($\Delta B_{z,c}$) in [pT]				
Slice	**Inferior**		**Superior**	
method	**No move**	**Jaw moved**	**No move**	**Jaw moved**
Residual	126 ± 12	175 ± 14	126 ± 33	168 ± 54
Control	104 ± 8	117 ± 12	81 ± 13	129 ± 42

Experiment 4: std($\Delta B_{z,c}$) in [pT] and median($\left\|\nabla\left(\Delta B_{z,c}\right)\right\|$) in [mA/m^2]				
Slice	**Inferior**		**Superior**	
method	**original**	**Improved**	**original**	**Improved**
$\Delta B_{z,c}$	163 ± 23	89 ± 16	154 ± 27	78 ± 7
$\left\|\nabla\left(\Delta B_{z,c}\right)\right\|$	124 ± 46	43 ± 10	79 ± 17	42 ± 7

Abbreviations: AW, acquisition-weighted; pT, picotesla.

The $\Delta B_{z,c}$ simulation based on the reconstructed cable paths are subtracted from the $\Delta B_{z,c}$ measurements to obtain residual images. Experiment 1: To explore the importance of proper spoiling in the $\Delta B_{z,c}$ measurements, the SDs of the $\Delta B_{z,c}$ residual images and of images from control measurements with no currents were compared for different spoiling schemes ([2 π-32 π] intravoxel dephasing employed without RF-spoiling and 16-π dephasing combined with RF-spoiling). The combination of RF and 16-π gradient spoiling performs best among the tested schemes in terms of SD. Experiment 2: Comparison of standard acquisition with no postfiltering applied and acquisition weighting (AW). Employing AW in the phase-encoding direction significantly improves the $\Delta B_{z,c}$ measurement sensitivity. Experiment 3: Impact of an intentional subject movement (jaw movement twice during the scan) on the $\Delta B_{z,c}$ measurement sensitivity. Significant increases of the noise floor were observed in both residual and control $\Delta B_{z,c}$ measurements caused by subject movement. Experiment 4: Our original method used in Göksu et al[9] is directly compared with our improved method in terms of $\Delta B_{z,c}$ measurement sensitivity and median of the norm of the current-induced field gradients $\left|\nabla\left(\Delta B_{z,c}\right)\right|$. The average SDs of $\Delta B_{z,c}$ images and their SDs across five subjects are given in [pT]. The average median values of $\left|\nabla\left(\Delta B_{z,c}\right)\right|$ images and their SDs across five subjects are given in [mA/m^2]. Our improved method shows more than 2-fold sensitivity increase for a matched total scan time.

In human experiments (see Figure 3B for the first subject's results and Supporting Information Figure S6 for all subjects), no severe artifacts are observed in the MR-magnitude images. The current-induced magnetic-field images qualitatively improve, and the spurious field fluctuation near ventricles along the phase-encoding direction vanishes in the AW images.

AW consistently reduces the noise floors of $\Delta B_{z,c}$ and the norm of its gradient $\left|\nabla\left(\Delta B_{z,c}\right)\right|$ for all subjects in both the residual images and control measurements without currents. On average across the three subjects, the noise SDs are reduced by 28% for the inferior slice and 18% for the superior slice in the residual $\Delta B_{z,c}$ images; and by 13% for the inferior slice and 46% for the superior slice in the control measurements without currents (Table 1).

3.4 | Experiment 3: Using navigators for data-quality assessment and exploring the influence on sensitivity

Discarding the first echo in the combined $\Delta B_{z,c}$ measurements of experiment 2 causes <1% increase in the noise floor, which shows that the first echo can be replaced with a navigator without penalty on SNR.

The $\Delta B_{z,c}$ measurements of the first subject in experiments with and without intentional jaw movements and the influence of the movements on the steady-state navigator-signal magnitude are shown in Figure 3C (see Supporting Information Figure S7 for the results of all subjects). The movements consistently cause peaks in the magnitude signal in all experiments (indicated by black dashed circles), whereas there are no significant phase variations observed in the navigator signal.

Jaw movements do not have a visually observable effect on the quality of the current-induced magnetic field $\Delta B_{z,c}$ and MR magnitude images. However, on average across the three subjects (Table 1), it increases the SDs by 39% for the inferior slice and 34% for the superior slice in the residual $\Delta B_{z,c}$ images, and by 13% for the inferior slice and 60% for superior slice in the control measurements without current injection.

3.5 | Experiment 4: Human in vivo brain MRCDI for two different current injection profiles

Figure 4A (subject 1) and Supporting Information Figure S8 (subjects 2–5) compare the $\Delta B_{z,c}$ measurements acquired with our original method[9] against our improved method. No significant artifacts are observed in the acquired MR-magnitude images. Our improved method lowers the $\Delta B_{z,c}$ noise floors in the 0-mA results consistently for every subject. In particular, it resolves the severe artifacts near ventricle regions in the inferior slice that occur for our original method (please note that only superior slices were measured in our initial study[9]). On average across the five subjects, the improved method exhibits an almost twofold sensitivity increase over our original method, with noise SDs in the $\Delta B_{z,c}$ images as low as 78 pT in the superior slices and 89 pT in the inferior slices (Table 1). The better quality of the improved method translates to lower noise floors in the images of the norm of the gradient $\left|\nabla\left(\Delta B_{z,c}\right)\right|$ (0 mA results in Figure 4B and Supporting Information Figure S9). Particularly severe noise near the ventricles in the inferior $\left|\nabla\left(\Delta B_{z,c}\right)\right|$ images is consistently avoided. On average across the five subjects, the improved method increases sensitivity 2.4-fold in the $\left|\nabla\left(\Delta B_{z,c}\right)\right|$ images, with noise medians as low as approximately 43 mA/m^2 in both slices (Table 1).

Also, for the measurements with 1-mA TES current injection, the improved method consistently achieves a higher SNR and better image quality. This is apparent in both the $\Delta B_{z,c}$ images (A→P montage in Figure 4A and Supporting Information Figure S8; R→L montage in Supporting Information Figure S10) and the current-flow reconstructions $\left|\vec{J}_{rec}\right|$ (A→P montage in Figure 4B and Supporting Information Figure S9; R→L montage in Supporting Information Figure S11). The improvements are most clearly seen in the regions near the ventricles that suffer from severe artifacts in the results obtained with our original method.

The correspondences between simulated and measured $\Delta B_{z,c}$ and simulated and measured reconstructed current flows (Figure 4 and Supporting Information Figures S8-S11) are tested quantitatively by linear regression, analogous to our previous study.[9] The intercepts β_0 are in acceptable ranges and the slopes β_1 are closer to 1 for our improved method (Figure 4C and Table 2). Our improved method shows consistent increases in the coefficients of determination for all subjects:

- Superior slice ($\Delta B_{z,c}$): $\Delta R^2 = 0.07$ for A→P and $\Delta R^2 = 0.08$ for R→L; inferior slice: $\Delta R^2 = 0.18$ for A→P and $\Delta R^2 = 0.14$ for R→L averaged across subjects.
- Superior slice (current flow): $\Delta R^2 = 0.17$ for A→P and $\Delta R^2 = 0.19$ for R→L; inferior slice: $\Delta R^2 = 0.32$ for A→P and $\Delta R^2 = 0.21$ for R→L averaged across subjects).

4 | DISCUSSION

We propose an improved gradient-echo–based MRCDI method with an optimized spoiling scheme, AW and navigators to reliably detect the tiny magnetic fields induced by TES in the human brain. The improvements successfully resolved several limitations of our prior approach[9]:

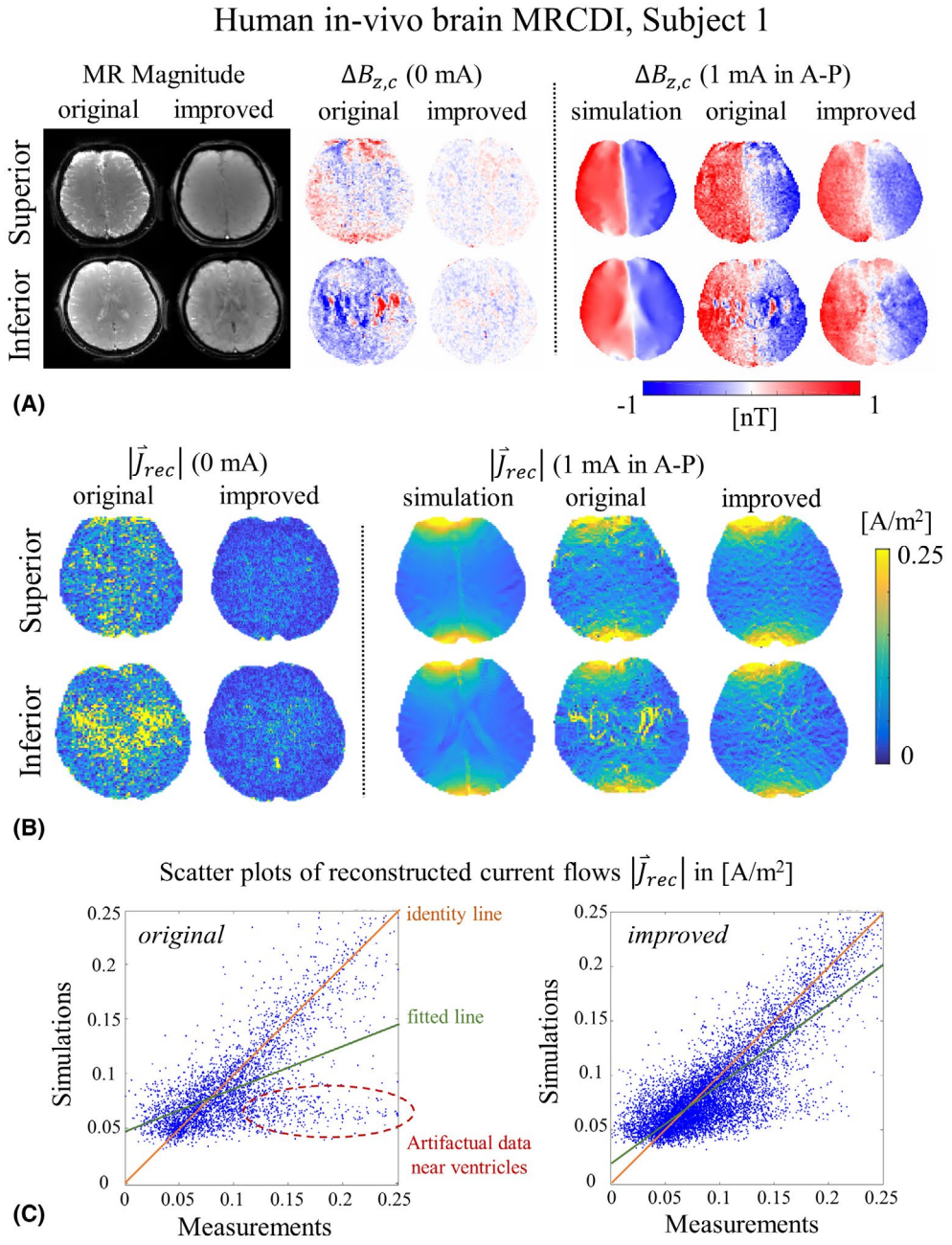

FIGURE 4 Experiment 4: Results for the first subject for the direct comparison of the final version of our improved magnetic resonance current-density imaging (MRCDI) measurement method with our original method.[9] A, The improved method significantly reduces the $\Delta B_{z,c}$ noise floors (0 mA results) and enhances the image quality and resolution of the $\Delta B_{z,c}$ measurements (1 mA A→P current injection). It also successfully resolves spurious $\Delta B_{z,c}$ variations occurring near ventricles. The $\Delta B_{z,c}$ simulations and measurements show similar distributions, and are in the same range. B, SNR and image-quality changes are more clearly observed in the current flow reconstructions based on $\Delta B_{z,c}$ measurements and simulations, where noise floors are strongly reduced for our improved method. The reconstructed current flows from the simulations are similar to the measurements. C, The scatter plots of the inferior slice results clearly show the relevance of the improved measurement method. The fitted line (green) approaches the identity line (orange) that is the ideal case. Our improved method also resolves the cluster (red) corresponding to the artifacts near ventricles. A-P, anterior to posterior

1. First, our experiments in phantoms and humans showed the importance of using stronger spoiling than normally needed for imaging. We used 2-mA currents (baseline to peak) in the LOOP-SETUP experiments to unambiguously assess the efficiency of the different spoiling approaches. In contrast, we applied only 1 mA when imaging the current flow induced by TES in the brain and the use of fat suppression was not allowing acquiring later echoes in our previous study,[9] so that the impact of insufficient spoiling was far less obvious. However, our new

TABLE 2 Experiment 4: The regression analyses to explore the correspondence between measurements and simulations based on realistic head models are given as averages across the five subjects: $\Delta B_{z,c}$ recordings and current flow reconstructions $|\vec{J}_{rec}|$

The regression analysis of $\Delta B_{z,c}$						
Method	**Original**			**Improved**		
Parameters	**β_0 in [pT]**	**β_1**	**R^2**	**β_0 in [pT]**	**β_1**	**R^2**
A→P						
Superior	40 ± 81	0.83 ± 0.12	0.77 ± 0.02	−33 ± 137	1.12 ± 0.10	0.84 ± 0.04
Inferior	28 ± 74	0.66 ± 0.12	0.61 ± 0.06	−92 ± 74	0.93 ± 0.11	0.79 ± 0.03
R→L						
Superior	2.4 ± 97	0.41 ± 0.13	0.31 ± 0.26	10 ± 140	0.75 ± 0.13	0.39 ± 0.22
Inferior	−31 ± 105	0.51 ± 0.09	0.37 ± 0.05	−61 ± 120	0.83 ± 0.19	0.51 ± 0.09
The regression analysis of $|\vec{J}_{rec}|$						
Method	**Original**			**Improved**		
Parameters	**β_0 in [mA/m^2]**	**β_1**	**R^2**	**β_0 in [mA/m^2]**	**β_1**	**R^2**
A→P						
Superior	22.6 ± 6.4	0.69 ± 0.09	0.61 ± 0.09	13.1 ± 1.6	0.83 ± 0.04	0.78 ± 0.05
Inferior	39.4 ± 6.7	0.44 ± 0.06	0.37 ± 0.07	18.8 ± 5.2	0.72 ± 0.10	0.69 ± 0.06
R→L						
Superior	19.7 ± 4.3	0.67 ± 0.07	0.64 ± 0.07	11.7 ± 1.8	0.82 ± 0.03	0.83 ± 0.04
Inferior	27.3 ± 7.2	0.53 ± 0.1	0.52 ± 0.13	14.8 ± 2.1	0.74 ± 0.04	0.73 ± 0.06

Abbreviation: pT, picotesla.

Linear fits of the measurements and simulations for the current injections in anterior→posterior (A→P) and right→left (R→L) directions are compared for our original and improved methods. The table lists the intercepts β_0, the slopes β_1, and the coefficient of determination R^2 of the fitted linear regression models (±SDs across the five subjects). The significances of the regression models were confirmed using F tests, with the results being highly significant ($P < 10^{-6}$) in all cases. Interestingly, the correspondence to the simulations consistently increases for our improved method, indicating the impact of an improved measurement SNR on the fitting accuracy. In particular, the artifacts observed near ventricles dramatically reduced the correspondence for the inferior slice measurements with our original method.

findings suggest that the current-induced field changes around small CSF-filled sulci reported in Göksu et al[9] may be exaggerated. Specifically, the results in Göksu et al[9] might have been influenced by residual effects of CSF flow and by the choice of the relaxation parameters in the steady-state models that is not accurate for CSF regions. Although spoiling used in Göksu et al[9] may provide better current-induced phase sensitivity in the CSF region that may improve current flow reconstruction in theory, the method is highly prone to modeling errors and impractical against enhanced spoiling.

2. Second, our results showed that acquisition of more echoes instead of employing fat suppression can improve the sensitivity of MRCDI measurements without compromising the image quality. The high bandwidth of the acquisition prevents the fat signal originating from the scalp and the fatty spongy bone of the skull from being shifted into the brain.
3. Third, AW efficiently resolved ringing artifacts caused by the sinc-shaped PSF of standard acquisition schemes. In direct comparison to our original method,[9] the new method achieves better sensitivity levels of the $\Delta B_{z,c}$ images and the reconstructed current-flow images in half of the scan time. The improved PSF shape seems particularly beneficial for the reconstruction of the current flow images, as this relies on spatial differentiation.
4. Lastly, our results established the feasibility of detecting undesired motion-induced signal fluctuations for quality control by replacing the first echo with a navigator, which causes a negligible SNR compromise. Here, it helped us to rule out the possibility that subject motion caused the discrepancies between $\Delta B_{z,c}$ simulations and measurements, which we observed for the R→L electrode configuration in some of the subjects.

4.1 | Comparison of measured and simulated fields

The correspondence between measurements and simulations notably increased for our improved method compared with

the original method, highlighting the relevance of the enhanced image quality.

Interestingly, the correspondence for the current-induced magnetic fields varied between the two electrode configurations (A→P: $\beta_1 = 1.03$, $R^2 = 0.82$; R→L: $\beta_1 = 0.79$, $R^2 = 0.45$, averaged across the five subjects and the two slice positions). Considering our careful validations of the MR measurement approach, it seems unlikely that these differences arose from limitations in the measured data. Rather, the results indicate that the employed volume conductor models (including the head, electrode pads, and gel) might be less accurate for simulations of the tested R→L electrode montage. Along similar lines, it is worth noting that the measured and simulated magnetic fields deviate clearly from each other near electrode regions in some of the experiments. Although beyond the scope of this study, these findings indicate that MRCDI provides useful data to potentially improve the accuracy of the field simulations, for example, by testing head models[54] with improved anatomical detail.[55]

In contrast to the current-induced magnetic fields, the current density images reconstructed from measurements and simulations showed a good correspondence that was similar for both current-injection profiles. Presumably, this is because of the loss of fine spatial details caused by the employed reconstruction method, as already observed in our prior study (ie, seen in Figure 8 in Göksu et al[9]). As of now, we thus consider the similarity between measured and simulated current-induced magnetic fields a more reliable measure of the fit of the simulated current flow.

4.2 | Prior studies, status, and future work

So far, only a few studies have reported successful MR recordings of the magnetic fields of TES currents induced in the human brain[9,29,30] based on MR methods with sufficient phase sensitivity. Although a mismatch between simulated and measured current-induced magnetic fields was still apparent as differences in spatial patterns and peak strengths in the results of two these studies,[29,30] this could be mostly resolved in Göksu et al[9] by correcting for the stray magnetic fields caused by the cable currents. Compared with the results in Göksu et al,[9] we here improved the sensitivity further, while we also enhanced the spatial resolution, reduced the sensitivity to CSF flow, and minimized the effect of different tissue-specific relaxation times on the estimated current-induced magnetic field changes. Those measures strongly improved the quality of the $\Delta B_{z,c}$ images and also resolved spurious artifacts that had previously remained also after correcting for the cable stray fields. The acquisition time was kept rather short here, which leaves room for further reduction of the noise levels by temporal averaging.

Considering the achieved sensitivity levels and robustness to physiological noise, we are optimistic that our improved method will be useful in characterizing individual current-flow patterns induced by TES. Although further advancing the MR imaging methods will still be relevant, we suggest that improving the reconstruction methods is at least equally important. For example, the reconstruction method employed here[18,56] resulted in rather coarse current-density images even when applied to noiseless simulated current-induced magnetic fields. This is in contrast to its performance reported for phantom measurements, and indicates the need to adapt the approach to the human head anatomy. Alternatively, conductivity reconstructions using the Laplacian $\nabla^2 \left(\Delta B_{z,c}\right)$ are less affected by stray magnetic fields originating from current flow outside the measured region, which might increase the stability of the reconstruction, in particular around electrode regions,[16,57] but its use is practically challenging because of strong noise amplification.

The MR phase images could be further improved in several ways. For example, balanced SSFP can in theory provide an even better sensitivity to the TES-induced field changes and is robust against physiological variations. However, its sensitivity to field inhomogeneities makes its use challenging.[58,59] Double-echo planar imaging[60] might help to reduce the sensitivity of the MR data to physiological field fluctuations, but likely has lower sensitivity to the current-induced magnetic fields. Furthermore, ultrahigh-field MRI, for example, at 7T or 9.4T, generally offers higher SNRs,[61] but also requires careful optimization of the imaging methods to achieve robust results.[62] Another important goal would be the extension to simultaneous multislice[63] or volume acquisition to obtain more complete information of the current-induced magnetic field changes, which might help the accurate reconstruction of the TES currents and the conductivity distribution in the brain. However, maintaining the required sensitivity levels, image quality, and robustness to physiological noise within a larger brain volume might be challenging.

5 | CONCLUSIONS

We have shown MRCDI measurements of the human brain with high sensitivity and high spatial resolution, providing high-quality maps of current-induced magnetic fields with minimized artifacts. Our results proved the importance to test for nonlinear dependencies of the MR signal phase on the current-related magnetic field changes that, if ignored, can cause systematic artifacts in the current-induced magnetic field images. We suggest that the achieved level of image quality and robustness to physiological noise will be beneficial to make MRCDI a reliable and accurate method for characterizing the individual current-flow patterns induced by TES.

ACKNOWLEDGMENTS

The financial support of the Lundbeck Foundation (grant nos. R288-2018-236 to C.G. and R244-2017-196 and R313-2019-622 to A.T.), the Max Planck Society, and the German Research Foundation (Reinhart Koselleck Project, DFG SCHE 658/12) is gratefully acknowledged. H.R.S. holds a 5-year professorship in precision medicine at the Faculty of Health Sciences and Medicine, University of Copenhagen, which is sponsored by the Lundbeck Foundation (grant no. R186-2015-2138).

CONFLICT OF INTEREST

Hartwig R. Siebner has received honoraria as speaker from Sanofi Genzyme, Denmark, and Novartis, Denmark; as consultant from Lundbeck, Denmark, Lophora, Denmark, Sanofi Genzyme, Denmark; and as editor-in-chief of *NeuroImage Clinical* and senior editor of *NeuroImage* from Elsevier Publishers, Amsterdam, The Netherlands. He has received royalties as book editor from Springer Publishers, Stuttgart, Germany, and Gyldendal, Copenhagen, Denmark. All other authors declare no conflicts of interest.

ORCID

Cihan Göksu https://orcid.org/0000-0002-6214-032X
Klaus Scheffler https://orcid.org/0000-0001-6316-8773
Fróði Gregersen https://orcid.org/0000-0002-0648-8399
Hasan H. Eroğlu https://orcid.org/0000-0002-8723-5894
Rahel Heule https://orcid.org/0000-0002-4589-6483
Hartwig R. Siebner https://orcid.org/0000-0002-3756-9431
Lars G. Hanson https://orcid.org/0000-0002-8204-6912
Axel Thielscher https://orcid.org/0000-0002-4752-5854

REFERENCES

1. Nitsche MA, Paulus W. Excitability changes induced in the human motor cortex by weak transcranial direct current stimulation. *J Physiol*. 2000;527:633-639.
2. Scott GC, Joy MLG, Armstrong RL, Henkelman RM. Sensitivity of magnetic-resonance current-density imaging. *J Magn Reson*. 1992;97:235-254.
3. Joy MLG. MR current density and conductivity imaging: the state of the art. In: Conf Proc IEEE Eng Med Biol Soc. Vol. 7. 2004. pp. 5315-5319.
4. Eyüboğlu BM. Magnetic resonance current density imaging. In: Akay M, ed. *Wiley Encyclopedia of Biomedical Engineering*. Vol. 4. Hoboken, New Jersey, United States: John Wiley & Sons, Inc; 2006, pp. 2147-2153.
5. Eyüboğlu BM. Magnetic resonance-electrical impedance tomography. In: Akay M, ed. *Wiley Encyclopedia of Biomedical Engineering*. Vol. 4. Hoboken, New Jersey, United States: John Wiley & Sons, Inc; 2006. pp. 2154-2162.
6. Sadleir RJ, Grant SC, Silver X, et al. Magnetic resonance electrical impedance tomography (MREIT) at 11 Tesla field strength. *Preliminary Experimental Study*. 2005;7:340-343.
7. Seo JK, Kwon O, Woo EJ. Magnetic resonance electrical impedance tomography (MREIT): conductivity and current density imaging. *J Phys Conf Ser*. 2005;12:140-155.
8. Seo JK, Woo EJ. Magnetic resonance electrical impedance tomography. *Soc Ind Appl Math*. 2011;53:40-68.
9. Göksu C, Hanson LG, Siebner HR, Ehses P, Scheffler K, Thielscher A. Human in-vivo brain magnetic resonance current density imaging (MRCDI). *Neuroimage*. 2018;171:26-39.
10. Göksu C, Scheffler K, Ehses P, Hanson LG, Thielscher A. Sensitivity analysis of magnetic field measurements for magnetic resonance electrical impedance tomography (MREIT). *Magn Reson Med*. 2018;79:748-760.
11. Sadleir R, Grant S, Zhang SU, et al. Noise analysis in magnetic resonance electrical impedance tomography at 3 and 11 T field strengths. *Physiol Meas*. 2005;26:875-884.
12. Hasanov KF, Ma AW, Yoon RS, Nachman AI, Joy ML. A new approach to current density impedance imaging. *Conf Proc IEEE Eng Med Biol Soc [Internet]*. 2004;2:1321-1324.
13. Birgül Ö, Eyüboğlu BM, Ider YZ. Experimental results for 2D magnetic resonance electrical impedance tomography (MR-EIT) using magnetic flux density in one direction. *Phys Med Biol*. 2003;48:3485-3504.
14. Sadighi M, Göksu C, Eyüboğlu BM. J-based magnetic resonance conductivity tensor imaging (MRCTI) at 3 T. In: Annual International Conference of the IEEE Engineering in Medicine and Biology Society—EMBC. 2014. pp. 1139-1142.
15. Ider YZ, Birgül Ö. Use of the magnetic field generated by the internal distribution of injected currents for electrical impedance tomography (MR-EIT). *ELEKTRİK*. 1998;6:215-225.
16. Oh SH, Il LB, Woo EJ, et al. Conductivity and current density image reconstruction using harmonic Bz algorithm in magnetic resonance electrical impedance tomography. *Phys Med Biol*. 2003;48:3101-3116.
17. Oh SH, Lee B, Woo EJ, et al. Electrical conductivity images of biological tissue phantoms in MREIT. *Physiol Meas*. 2005;26:S279-S288.
18. Woo EJ, Seo JK. Magnetic resonance electrical impedance tomography (MREIT) for high-resolution conductivity imaging. *Physiol Meas*. 2008;29:R1-R26.
19. Minhas AS, Jeong WC, Kim YT, Han Y, Kim HJ, Woo EJ. Experimental performance evaluation of multi-echo ICNE pulse sequence in magnetic resonance electrical impedance tomography. *Magn Reson Med*. 2011;66:957-965.
20. Jeon K, Lee C, Kim H, Woo E. CoReHA: conductivity reconstructor using harmonic algorithms for magnetic resonance electrical impedance tomography (MREIT). *J Biomed Eng*. 2009;30:279-287.
21. Han YQ, Meng ZJ, Jeong WC, et al. MREIT conductivity imaging of canine head using multi-echo pulse sequence. *J Phys Conf Ser*. 2010;224:012078.
22. Kim HJ, Oh TI, Kim YT, et al. In vivo electrical conductivity imaging of a canine brain using a 3 T MREIT system. *Physiol Meas*. 2008;29:1145-1155.
23. Jeong WC, Sajib SZK, Katoch N, Kim HJ, Kwon OI, Woo EJ. Anisotropic conductivity tensor imaging of in vivo canine brain using DT-MREIT. *IEEE Trans Med Imaging*. 2017;36:124-131.
24. Kim HJ, Jeong WC, Kim YT, et al. In vivo conductivity imaging of canine male pelvis using a 3T MREIT system. *J Phys Conf Ser*. 2010;224:4.
25. Jeong WC, Kim YT, Minhas AS, et al. In vivo conductivity imaging of human knee using 3 mA injection current in MREIT. *J Phys Conf Ser*. 2010;224:012148.
26. Meng Z, Sajib SZ, Chauhan M, et al. Improved conductivity image of human lower extremity using MREIT with chemical shift artifact correction. *Biomed Eng Lett*. 2012;2:62-68.

27. Kim HJ, Kim YT, Minhas AS, et al. In vivo high-resolution conductivity imaging of the human leg using MREIT: the first human experiment. *IEEE Trans Med Imaging*. 2009;28:1681-1687.
28. Kim YT, Minhas AS, Meng Z, Kim HJ, Woo EJ. Conductivity imaging of human lower extremity using MREIT with multi-echo pulse sequence and 3 mA imaging current. 8th Int. Symp. Noninvasive Funct. Source Imaging Brain Hear. 8th Int. Conf. Bioelectromagn. 2011, pp. 48-52.
29. Chauhan M, Indahlastari A, Kasinadhuni AK, Schar M, Mareci TH, Sadleir RJ. Low-frequency conductivity tensor imaging of the human head in vivo using DT-MREIT: first study. *IEEE Trans Med Imaging*. 2018;37:966-976.
30. Kasinadhuni AK, Indahlastari A, Chauhan M, Scär M, Mareci TH, Sadleir RJ. Imaging of current flow in the human head during transcranial electrical therapy. *Brain Stimul*. 2017;10:764-772.
31. Jog MV, Smith RX, Jann K, et al. In-vivo imaging of magnetic fields induced by transcranial direct current stimulation (tDCS) in human brain using MRI. *Sci Rep*. 2016;6:34385.
32. Antal A, Alekseichuk I, Bikson M, et al. Low intensity transcranial electric stimulation: safety, ethical, legal regulatory and application guidelines. *Clin Neurophysiol*. 2017;128:1774-1809.
33. Göksu C, Scheffler K, Siebner HR, Thielscher A, Hanson LG. The stray magnetic fields in magnetic resonance current density imaging (MRCDI). *Eur J Med Phys*. 2019;59:142-150.
34. Walsh DO, Gmitro AF, Marcellin MW. Adaptive reconstruction of phased array MR imagery. *Magn Reson Med*. 2000;43:682-690.
35. Lee H, Jeong WC, Kim HJ, Woo EJ, Park J. Alternating steady state free precession for estimation of current-induced magnetic flux density: a feasibility study. *Magn Reson Med*. 2016;75:2009-2019.
36. Jaynes ET. Matrix treatment of nuclear induction. *Phys Rev*. 1955;98:1099-1105.
37. Preibisch C, Deichmann R. Influence of RF spoiling on the stability and accuracy of T1 mapping based on spoiled FLASH with varying flip angles. *Magn Reson Med*. 2009;61:125-135.
38. Nam HS, Kwon OI. Optimization of multiply acquired magnetic flux density B(z) using ICNE-Multiecho train in MREIT. *Phys Med Biol*. 2010;55:2743-2759.
39. Gregersen F, Göksu C, Schaefers G, Xue R, Thielscher A, Hanson LG. Safety evaluation of a new setup for transcranial electric stimulation during magnetic resonance imaging. *Brain Stimul*. 2021;14:488-497.
40. Pohmann R, von Kienlin M. Accurate phosphorus metabolite images of the human heart by 3D acquisition-weighted CSI. *Magn Reson Med*. 2001;45:817-826.
41. Budde J, Shajan G, Scheffler K, Pohmann R. Ultra-high resolution imaging of the human brain using acquisition-weighted imaging at 9.4T. *Neuroimage*. 2014;86:592-598.
42. Haase A, Frahm J, Hänicke W, Matthaei D. 1H NMR chemical shift selective (CHESS) imaging. *Phys Med Biol*. 1985;30:341-344.
43. Dietrich O, Raya JG, Reeder SB, Reiser MF, Schoenberg SO. Measurement of signal-to-noise ratios in MR images: influence of multichannel coils, parallel imaging, and reconstruction filters. *J Magn Reson Imaging*. 2007;26:375-385.
44. Sadleir R, Grant S, Zhang SU, et al. Noise analysis in magnetic resonance electrical impedance tomography at 3 and 11 T field strengths. *Physiol Meas*. 2005;26:875-884.
45. Ida M, Wakayama T, Nielsen ML, Abe T, Grodzki DM. Quiet T1-weighted imaging using PETRA: initial clinical evaluation in intracranial tumor patients. *J Magn Reson Imaging*. 2015;41:447-453.
46. Nielsen JD, Madsen KH, Puonti O, et al. Automatic skull segmentation from MR images for realistic volume conductor models of the head: assessment of the state-of-the-art. *Neuroimage*. 2018;174:587-598.
47. Thielscher A, Antunes A, Saturnino GB. Field modeling for transcranial magnetic stimulation: a useful tool to understand the physiological effects of TMS? In: Proceedings of the Annual International Conference of the IEEE Engineering in Medicine and Biology Society, EMBS. 2015. pp. 222-225.
48. Thielscher A, Opitz A, Windhoff M. Impact of the gyral geometry on the electric field induced by transcranial magnetic stimulation. *Neuroimage*. 2011;54:234-243.
49. Wagner TA, Zahn M, Grodzinsky AJ, Pascual-Leone A. Three-dimensional head model simulation of transcranial magnetic stimulation. *IEEE Trans Biomed Eng*. 2004;51:1586-1598.
50. Saturnino GB, Antunes A, Thielscher A. On the importance of electrode parameters for shaping electric field patterns generated by tDCS. *Neuroimage*. 2015;120:25-35.
51. Yazdanian H, Saturnino GB, Thielscher A, Knudsen K. Fast evaluation of the Biot-Savart integral using FFT for electrical conductivity imaging. *J Comput Phys*. 2020;411:1-7.
52. Park C, Il LB, Kwon OI. Analysis of recoverable current from one component of magnetic flux density in MREIT and MRCDI. *Phys Med Biol*. 2007;52:3001-3013.
53. Jeong WC, Sajib SZK, Kim HJ, Kwon OI. Focused current density imaging using internal electrode in magnetic resonance electrical impedance tomography (MREIT). *IEEE Trans Biomed Eng*. 2014;61:1938-1946.
54. Eroğlu HH, Puonti O, Göksu C, et al. *On the Reconstruction of Magnetic Resonance Current Density Images of the Human Brain: Pitfalls and Perspectives*. bioRxiv. Cold Spring Harbor, NY, United States: Cold Spring Harbor Laboratory; 2021.
55. Puonti O, Van Leemput K, Saturnino GB, Siebner HR, Madsen KH, Thielscher A. Accurate and robust whole-head segmentation from magnetic resonance images for individualized head modeling. *Neuroimage*. 2020;219:117044.
56. Nam HS, Park C, Kwon OI. Non-iterative conductivity reconstruction algorithm using projected current density in MREIT. *Phys Med Biol [Internet]*. 2008;53:6947-6961.
57. Seo JK, Yoon J, Woo EJ, Kwon O. Reconstruction of conductivity and current density images using only one component of magnetic field measurements. *IEEE Trans Biomed Eng*. 2003;50:1121-1124.
58. Bieri O, Maderwald S, Ladd ME, Scheffler K. Balanced alternating steady-state elastography. *Magn Reson Med*. 2006;55:233-241.
59. Minhas AS, Member S, Woo EJ, Lee SY. Magnetic flux density measurement with balanced steady state free precession pulse sequence for MREIT: a simulation study. 2009;2276-2278.
60. Jog AMS, Jann K, Yan L, Yu H, Parra L, Narr K. Concurrent imaging of markers of current flow, brain-state and neurophysiological changes during tDCS Abstract. *Front Neurosci*. 2020;14:1-13.
61. Pohmann R, Speck O, Scheffler K. Signal-to-noise ratio and MR tissue parameters in human brain imaging at 3, 7, and 9.4 tesla using current receive coil arrays. *Magn Reson Med*. 2016;75:801-809.
62. Minhas AS, Chauhan M, Fu F, Sadleir R. Evaluation of magnetohydrodynamic effects in magnetic resonance electrical impedance tomography at ultra-high magnetic fields. *Magn Reson Med*. 2019;81:2264-2276.

63. Barth M, Breuer F, Koopmans PJ, Norris DG, Poser BA. Simultaneous multislice (SMS) imaging techniques. *Magn Reson Med*. 2016;75:63-81.

SUPPORTING INFORMATION

Additional Supporting Information may be found online in the Supporting Information section.

FIGURE S1 Schematic diagram of a gradient-echo-based MRCDI sequence (see the "Methods" section and (10,11) for details). Please note that, in case of a perfectly spoiled sequence, $\Delta\varphi_{ss} = 0$ so that the current injection could be stopped after acquisition of the last gradient echo without loss of sensitivity

FIGURE S2 Experiment S.1: Importance of proper spoiling. (i) Signal losses near pipes are observed in the MR magnitude image of the spherical phantom, mainly due to local field inhomogeneities lowering the T_2^*. (ii) Images of $\Delta B_{z,c}$ and its noise floor are exemplarily shown for the combination of RF and 16π gradient spoiling. (iii) Residual $\Delta B_{z,c}$ images (measurements with simulations of cable-induced fields subtracted) are shown for different spoiling schemes, and are expected to be zero ideally. The residual images with no RF-spoiling exhibit strong misestimations of $\Delta B_{z,c}$ in the regions that have low T_2^*. The combination of RF and 16π gradient spoiling minimizes the residuals

FIGURE S3 Experiment S.2: Sensitivity improvement by means of Acquisition weighting (AW). Combined MR magnitude images for standard and acquisition-weighted acquisitions, with alignment of the cylindrical tube in right-left R-L or anterior-posterior A-P direction. The impact of a better PSF is barely visible in the MR magnitude images (the green rectangles show the regions used for SNR calculations reported in Supporting Information Table S2; the red rectangles show the positions of the zoomed regions used in Figure 2C). AW improves the noise floors of the $\Delta B_{z,c}$ images

FIGURE S4 Experiment S.1: Control experiments without any currents. MR magnitude signal reduces for later echoes and show local signal losses near phantom edges due to the field inhomogeneities as expected. The $\Delta B_{z,c}$ noise images calculated for each of the echoes demonstrate a spatial distribution similar to random noise

FIGURE S5 Experiment 1: Importance of proper spoiling in human in vivo brain MRCDI. The results of both superior and inferior slice measurements of all subjects. Spurious local increases in the residual $\Delta B_{z,c}$ images near sulci and ventricles are consistently resolved by the combination of RF and 16π gradient spoiling (simulations subtracted from the magnetic fields measurements performed with LOOP-SETUP; ideally zero)

FIGURE S6 Experiment 2: Standard vs. acquisition-weighted (AW) human in vivo brain MRCDI. The results are shown for measurements of superior and inferior brain slices for all subjects. Images of the norm of the gradient of the current-induced magnetic field $\left|\nabla\left(\Delta B_{z,c}\right)\right|$ are shown. Residual images (simulations subtracted from the magnetic fields measurements performed with LOOP-SETUP) are compared with control measurements without current flow, and similar noise floors are observed. Employing AW improves the resolution and the noise floors significantly compared to the standard acquisition scheme

FIGURE S7 Experiment 3: Navigators. The results are shown for measurements of upper and lower brain slices for all subjects. The measurements for two conditions are compared: The subject performs no intentional movement (No-move) versus intentional jaw movements twice during the scan (Jaw-moved). (A) Jaw movement-induced noise floor increases in the $\Delta B_{z,c}$ measurements are marginally observable. (B) The MR magnitude signal acquired from the navigator fluctuates during the two jaw movements, and stays constant for the rest of the scan (here we show only the control measurements without current flow, as the results were similar for the recordings with current flow). The results are consistent over subjects

FIGURE S8 Results for the remaining four subject of experiment 4 for 0 mA and 1 mA A-P current injections (see Figure 4A for the first subject). The improved method significantly reduces the $\Delta B_{z,c}$ noise floors, enhances the image quality and resolution and successfully resolves spurious $\Delta B_{z,c}$ variations near ventricles. The $\Delta B_{z,c}$ measurements and simulations generally agree well, but show slight differences near electrodes. Both simulations and measurements are in the same range. The results are consistent among all five subjects

FIGURE S9 Current flow reconstructions for the remaining four subject of experiment 4 for 0 mA and 1 mA A-P current injections (see Figure 4B for the first subject). Noise floors decrease markedly for the improved method and the artifacts near ventricles are resolved. This consistently improves the correspondence between the current flows reconstructed from the simulations and the measurements

FIGURE S10 Experiment 4: Human in vivo brain MRCDI measurements and simulations for both the superior and inferior slices. The performance of our original method is directly compared with our improved method based on measurements with TES currents injected in anterior-posterior R-L direction. The measurements are consistent, but the improved method significantly reduces the $\Delta B_{z,c}$ noise floors, and enhances the image quality and resolution. Analogous to the A-P results, our improved method successfully resolves the artifacts near ventricles. The $\Delta B_{z,c}$ simulations and measurements for R-L are also in the same range, but show more differences in their spatial patterns when compared to the A-P results. The dependence of TES simulation accuracy on the injection configuration is beyond the scope of this study

FIGURE S11 Experiment 4: Human in vivo brain MRCDI current flow reconstructions based on $\Delta B_{z,c}$ measurements and simulations for both the superior and inferior slices. The performance of our original method is directly compared with our improved method based on measurements with TES currents injected in anterior-posterior R-L direction. Our improved method greatly improves the noise floors and enhances the image quality and resolution. Analogous to the A-P results, our improved method successfully resolves the artifacts near ventricles. The reconstructed current flows from the simulations agree well with the measurements, but generally lack detailed spatial information. Compared to $\Delta B_{z,c}$, the simulated and measured current flow reconstructions show more similar distributions, which may also be caused by the approximations used in the projected current density reconstruction algorithm

TABLE S1 Experiment S.1: Control measurements without any current. MR magnitude image SNR are given for every individual echo and their weighted combination. The calculated noise standard deviations based on SNR measurements are compared with the noise standard deviations derived from the $\Delta B_{z,c}$ measurements. The theoretical noise floors based on SNR measurements agree well with directly measured $\Delta B_{z,c}$ noise floors

TABLE S2 Experiment S.2: Anterior-posterior and right-left alignment of the phantom. Control measurements without any current. MR magnitude image SNR are given for every individual echo and their weighted combination. The calculated noise standard deviations based on SNR measurements are compared with the noise standard deviations derived from the $\Delta B_{z,c}$ measurements. The results are given for both acquisition schemes, standard vs. acquisition-weighted

How to cite this article: Göksu C, Scheffler K, Gregersen F, et al. Sensitivity and resolution improvement for in vivo magnetic resonance current-density imaging of the human brain. *Magn Reson Med.* 2021;86:3131–3146. https://doi.org/10.1002/mrm.28944